PROCEEDINGS, 50th Workshop on Geothermal Reservoir Engineering
Stanford University, Stanford, California, February 10-12, 2025
SGP-TR-229

Petrologic Validation of Exploration Geophysical Anomalies Utilizing Drill Core and Cuttings from the Don A. Campbell Geothermal System, Nevada, USA

Kurt O. Kraal[1], Matthew Folsom[2], Carmen Winn[2], Daniel Feucht[3], Ben Delwiche[3], Nicholas Hinz[2], William Cumming[4] Steve Sewell[5], & Christine Downs[1]

[1]Sandia National Laboratories, 1515 Eubank Blvd SE, Albuquerque, NM, 87123

[2] Geologica Geothermal Group Inc.

[3]Ormat Technologies Inc.

[4]Cumming Geoscience.

[5]Australis Geoscience Ltd.

E-mail: kokraal@sandia.gov

Keywords: Clay Cap, Smectite, BRIDGE, Silicification, Resistivity, HTEM, SWIR, Infrared Spectroscopy

ABSTRACT

Blind or hidden geothermal systems have been identified as an underutilized source of renewable energy in the Great Basin region of the western USA and developing techniques and strategies to detect such resources is an active area of research. The US DOE BRIDGE project has identified several petrophysical patterns that are associated with resource-capable geothermal systems in the Great Basin region that can be detected by geophysical methods like magnetotelluric (MT), gravity and aeromagnetic surveys. These include detecting low resistivity hydrothermal smectite alteration above the water table, densification of sediments due to precipitation of silica along cooling geothermal outflows, and variation in magnetite content of sediments due to hydrothermal alteration. Although geophysical interpretations have been plausibly attributed to hydrothermal alteration and precipitation, few publications report systematic analyses of subsurface samples to validate the petrologic basis for these geophysical interpretations in the moderate temperature (~120-200°C) deep circulation systems commonly found in the Great Basin.

Here we present results of petrologic analyses of core and cuttings from the Don A Campbell geothermal field to validate our interpretation of gravity and aeromagnetic data that was already available for this area and Helicopter Transient Electromagnetic (HTEM) resistivity data collected for the BRIDGE project over the site. This field currently produces from a shallow 120 to 130 °C outflow reservoir hosted in basin-fill sediments. The sample analysis methods utilized include sample inspection, infrared reflectance spectroscopy in the Short-Wave InfraRed range (SWIR), and Methylene-Blue (MeB) analysis to estimate smectite abundance. These results are integrated with supporting geologic and temperature data in the context of the natural state conceptual model for the reservoir. We found several hydrothermal alteration minerals that are relevant to the interpretation, including smectite, interlayered illite-smectite, kaolinite, silica, carbonate, hematite, and pyrite. These minerals are found with a distinct zonation with common hydrothermal alteration mineral assemblages, including a shallow smectite-bearing argillic zone, a shallow silica-carbonate-pyrite-illite-smectite zone embedded within the argillic zone, a deeper silica-carbonate-pyrite-illite-smectite with minor chlorite zone, and a shallow kaolinite-smectite-hematite zone near the water table. The relative smectite content of each of these zones can be inferred from the HTEM, with low-resistivity (from ~3 to 5 ohm.m) zones correlated with the argillic zone containing from 5 to 13% smectite, and relatively high-resistivity values (from ~5 to 7.5 ohm.m) correlated with the silica-carbonate-pyrite-illite-smectite zones that have smectite content less than 3%. In addition, the highest values in the first-derivative of the gravity data, inferred to be due to near-surface densification, correspond to the shallow silicified zone identified in the core and cuttings. These results are applicable to the interpretation of the regional HTEM and aeromagnetic data.

1. INTRODUCTION

In recent years, the geophysical methods most commonly used to explore specific geothermal prospects in the Great Basin are resistivity (especially MT), gravity and aeromagnetic surveys. Historically such exploration methods focused on prospects where some surface manifestation like a hot spring or active alteration indicated elevated subsurface temperature. However, as almost all prospects with such features in the Great Basin have been explored and developed, attention has shifted to hidden/blind systems that lack surface manifestations. The US Department of Energy's Geothermal Technologies Office (DOE-GTO) has funded several projects to develop strategies and methods to cost-effectively explore hidden geothermal systems in the Great Basin region, including the BRIDGE project (Downs et al., 2025) that acquired regional Helicopter Transient Electromagnetic (HTEM) resistivity data over and near Department of Defense lands in Nevada that earlier Play Fairway projects had identified as being prospective (Figure 1).

The use of resistivity surveys for geothermal exploration is informed by a conceptual model based on results from known geothermal systems in which shallow (from 0 to 1000 m) low resistivity zones (<5, <10 or <20 ohm.m, depending on geological context) have characteristic patterns that are consistent with a low resistivity, impermeable smectite clay zone capping the buoyant hot hydrothermal upflow and outflow hosted mainly in fracture-permeability of relatively resistive rocks. The low resistivity smectite clay is formed above the water table through hydrothermal alteration and below the water table through hydrothermal, diagenetic and sedimentary processes. In the Great Basin, very low resistivity (< 2 ohm.m) detected at depths shallower than 1000 m is typically associated with either hydrothermal smectite alteration or evaporitic sediments that contain smectite (Sewell et al., 2023). The correlation of low resistivity smectite clay with the impermeable zone that caps geothermal reservoirs worldwide had been initially discovered in the late-1970s by researchers investigating well cuttings and cores to interpret resistivity well log results at geothermal reservoirs in the Great Basin and the Salton Trough (Ershaghi et al., 1981; Rigby F. and Zebal, 1981). However, up to the mid-2000s, geophysical surveys directed at imaging the low resistivity smectite cap of geothermal reservoirs had been focused mainly on exploring potentially larger capacity >240°C geothermal resources hosted in volcanic settings (e.g. DiPippo, 2024; Cumming and Matson, 2021; Ussher et al., 2000). Since the mid-2000s, MT has been widely used to image low-resistivity zones interpreted as a smectite cap above and adjacent to moderate temperature (130-200°C) deep-circulation geothermal systems in the Great Basin region, for example, at San Emidio (Folsom et al., 2018, 2020), Bradys and Desert Peak (Folsom et al., 2018), Dixie Meadows (Delwiche et al., 2023), and Steamboat (Feucht et al., 2023). However, petrophysical constraints on these resistivity observations in the Great Basin have been given relatively little attention since the 1970s and the shallow details of the resistivity patterns detected by MT in the Great Basin include complexity that is unlikely to be related to smectite content. This issue has been highlighted by the BRIDGE HTEM resistivity surveys that have much higher resolution than MT surveys at shallow depths (e.g. Folsom et al., 2024). The petrophysical analyses presented here provide a more detailed understanding of the resistivity patterns detected by these HTEM and MT surveys and support the exploration strategy developed by BRIDGE for discovering hidden geothermal resources in the Great Basin. Although cost would likely prohibit mobilization of an HTEM system to explore a single geothermal prospect, a regional HTEM survey similar to the data acquired for BRIDGE is being acquired over most of the Great Basin as part of the USGS Earth Mapping Resource Initiative (Lederer et al., 2024).

The BRIDGE HTEM results have been integrated into an exploration strategy that includes detailed surface geology, LiDAR, 2 m temperature surveys, and well data in addition to other geophysical methods, including MT to extend HTEM results to greater depth and gravity and magnetic surveys. In a Great Basin geothermal exploration context, gravity methods are commonly utilized both for identifying and characterizing faults that offset lithology with contrasting density, and identifying near-surface densification related to silicification by hydrothermal fluids, as shown at San Emidio (Folsom et al., 2020). Aeromagnetic data are also used both to infer geologic framework, including faults, and to identify areas of possible hydrothermal alteration leading to the destruction of magnetite in acidic zones (Allis, 1990) or deposition of magnetite in other cases. The analyses of cuttings and core conducted in this project have support the petrophysical basis of the interpretation strategy developed by the BRIDGE project.

In order to better understand these geophysical tools, we conducted a petrologic investigation of drill core and cuttings that intersect these geophysical features. One location with an abundance of available geologic, geophysical, and well data is the Don A. Campbell (DAC) geothermal system in western Nevada, operated by Ormat Technologies, Inc. (Figure 1). The goal of this paper is to validate the interpretation of the HTEM data acquired over the site by the BRIDGE project by petrologic investigations of several geothermal wells and boreholes from the site. In this pilot project, we performed sample inspection, infrared reflectance spectroscopy analysis, and Methylene-blue analysis of drill core or cuttings from four wells. Follow up work could include petrographic microscopy, XRD analysis, and measurement of petrophysical properties (such as resistivity, density, magnetic susceptibility) for further validation.

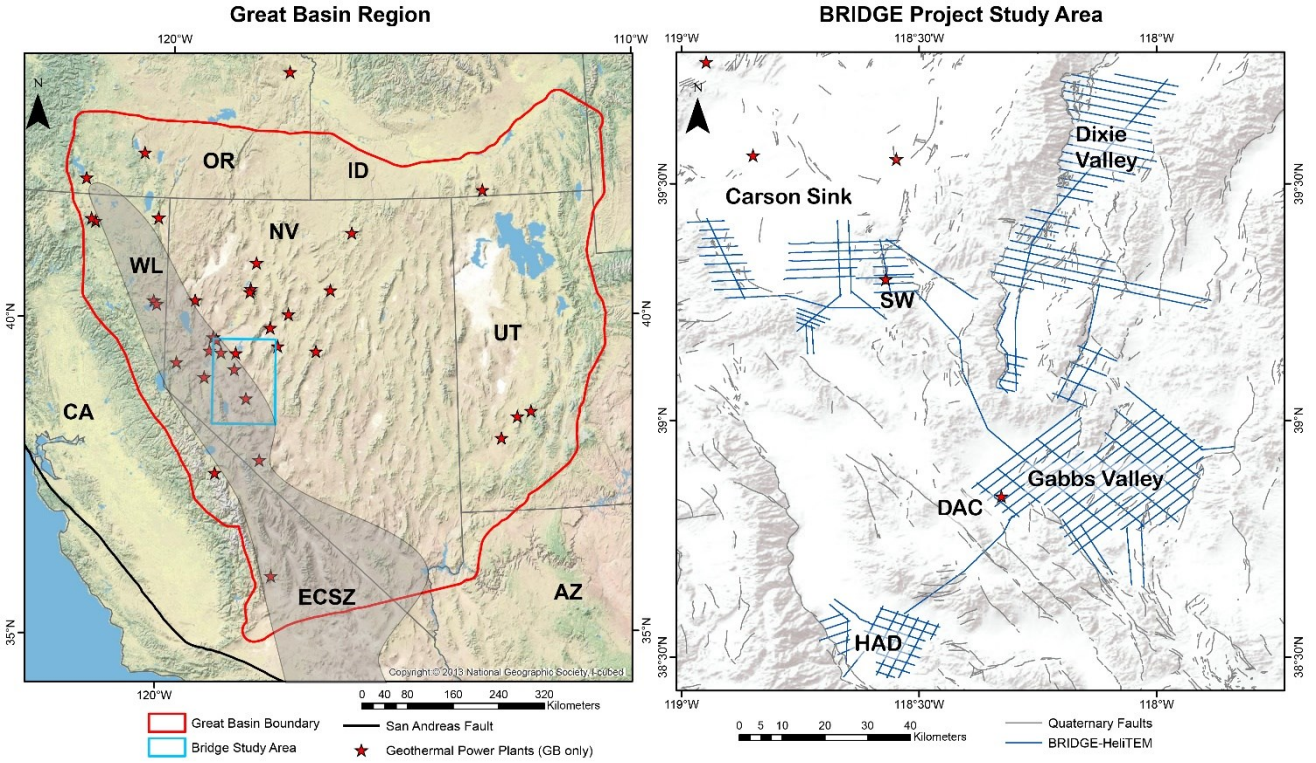

Figure 1: Left: Regional location of Great Basin (GB) region of the western USA, including the Walker Lane (WL) and Eastern California Share Zone (ECSZ), and the BRIDGE project study area. Right: Bridge project study area with locations of BRIDGE HeliTEM (HTEM) data acquisition, major basins investigated, and the location of the Don A. Campbell (D.A.C.) geothermal system. Also shown is the Salt Wells (SW) geothermal system location, and the Hawthorne Army Depot (HAD).

2. BACKGROUND

The Don A. Campbell (DAC) geothermal resource is located in Gabbs Valley of western Nevada. Gabbs Valley is within a transition between the Walker Lane, characterized by NW-striking dextral transtension that accommodates ~20% of the relative plate motion between the North American and Pacific Plates, and the Basin and Range province, characterized by northwest-southeast extension accommodated by northeast-striking normal faults (Figure 1). In addition to DAC, several other temperature anomalies have been identified in the basin, including blind geothermal system in southeast Gabbs Valley (Craig et al., 2021), Cobble Cuesta (Payne, 2013), North Gabbs (Kratt et al., 2008), and several additional hot wells near the town of Gabbs (Downs et al., 2023).

The DAC geothermal resource was discovered by investigating mineral exploration data from the early 1990s that identified a magnetic-low anomaly. Subsequently, hydrothermal alteration minerals such as clay, pyrite, chalcedony, and chlorite, and 88°C (190°F) fluids at depths between 50-500 ft were discovered through exploration drilling (Orenstein & Delwiche, 2014). Based on these data, Ormat nominated this property to the BLM's competitive geothermal lease auction in 2001, and secured site control in 2007. Ormat then commenced an exploration campaign, which included collection and interpretation of geoscientific data, drilling, and well production-injection testing. Following exploration, Ormat designed and installed a >16 MW (net) binary geothermal power plant that began production in 2013 (Orenstein & Delwiche, 2014). A second power plant was added in 2015, resulting in a generating capacity of 30 MW as of February 2024.

The DAC geothermal resource is located within a displacement transfer zone consisting of a series of northwest-striking oblique slip faults separated by northwest striking normal faults, some dipping to the northwest and others to the southeast (Delwiche, 2013; Figure 2A). A shallow (2-m) temperature survey conducted by Kratt et al. (2010) outlined a 6 km2 zone of elevated temperatures with maximum measured temperatures of 37°C (19.3°C above local background conditions; Figure 2A) consistent with and expanding the shallow temperature anomaly defined by the early geothermal exploration wells. A gravity survey identified shallow densification, as visible in the first vertical derivative (1VD) of the gravity data that is co-located with the shallow thermal anomaly (Feucht et al., 2024); Figure 2C). Ground magnetic data, as well as recent regional aeromagnetic data acquired as part of the GeoDAWN survey (Glen & Earney, 2024) both reveal a magnetic low that is co-located with the shallow temperature anomaly, and the shallow densification as observed in the gravity data (Figure 2D). Finally, the shallow resistivity data collected using HTEM by the BRIDGE project indicates a shallow (<100 m) low resistivity zone that is also co-located with the field as outlined by the shallow temperature data, exploration data, and the existing geophysical surveys (Sewell et al., 2023; Figure 2B).

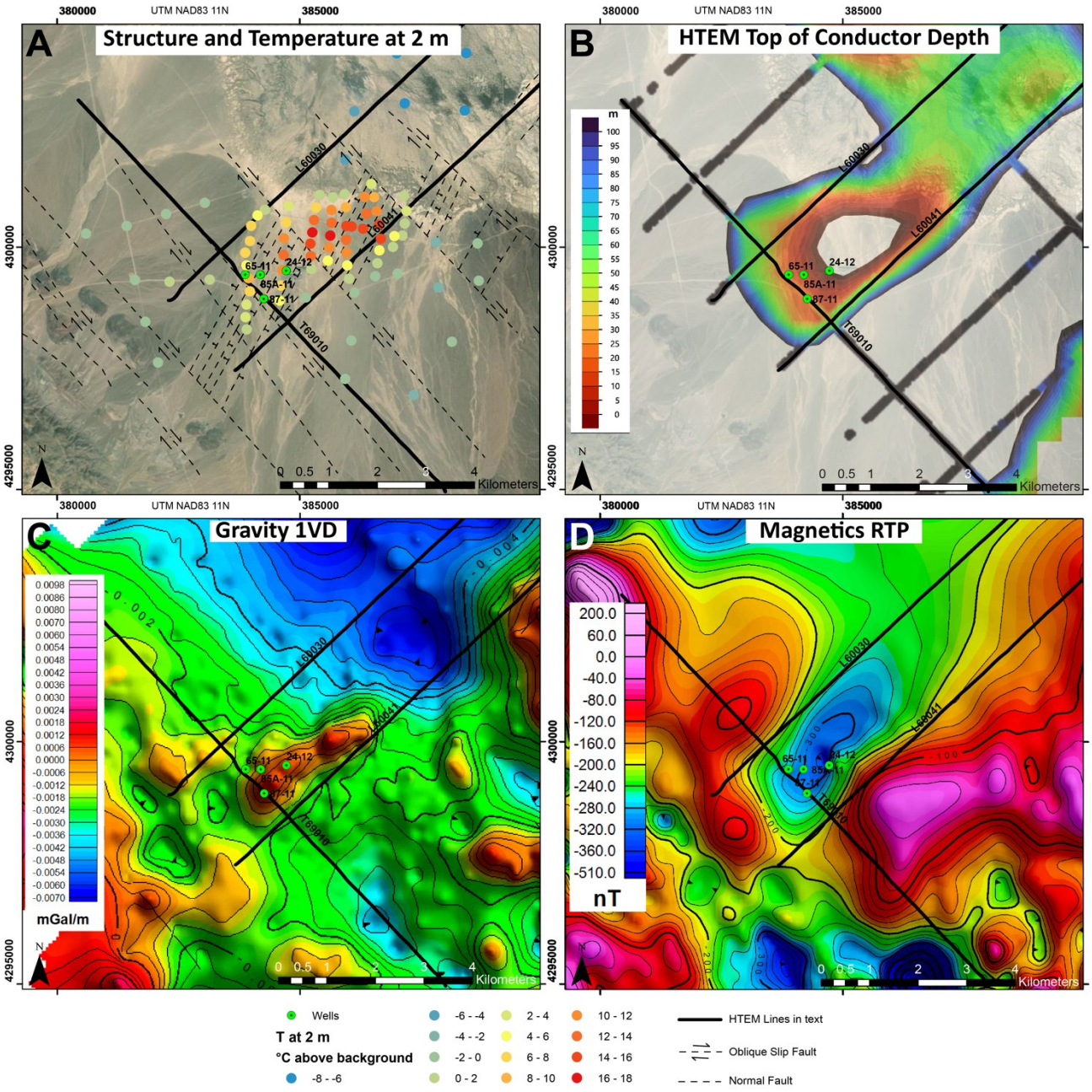

Figure 2: Maps of Don Campbell showing geophysics, cross section line, and well locations (for wells referenced in the text). A: Faults adapted from Delwiche (2013), and 2-m temperature survey from Kratt et al., (2010). B: HTEM top of conductor depth below surface from Sewell et al., (2023). C: Gravity 1VD from Feucht et al. (2024). D Magnetics RTP from GeoDAWN (Glen and Earney, 2024).

Three of the BRIDGE HTEM lines (L69010E, L60041N, L60030N) cross over the DAC geothermal resource (Figure 2, Figure 3). HTEM line L69010E runs roughly parallel to the northwest-striking oblique slip faults and crosses closest to the production wells currently in use at DAC (Figure 2). This line features a low resistivity zone (<3 ohm.m) at shallow depths (30 – 250 m) that is collocated with the magnetic low from GeoDAWN and the high in the Gravity 1VD (Figure 4). A portion of the shallow low resistivity zone in L69010E contains an embedded resistive zone (Figure 3). A portion of the HTEM data from this line was unusable where the survey crossed power plant infrastructure at DAC (shown as a vertical white area). HTEM line L60041N is perpendicular to L69010E and runs roughly parallel to the northwest striking normal faults just to the southeast of the wellfield (Figure 2). The HTEM section shows two domal-shaped shallow low resistivity zones that are divided by a northeast-striking oblique slip fault (Figure 2; Figure 3). HTEM line L60030N is parallel to L60041N, and passes just to the northwest of the DAC wellfield (Figure 2). This line also has a shallow low resistivity zone in two layers surrounding an embedded resistive body (Figure 3). Because L69010E most directly crosses the resource, existing geothermal wells, and the geophysical anomalies of interest, we will restrict our discussion to this line for the purposes of this study.

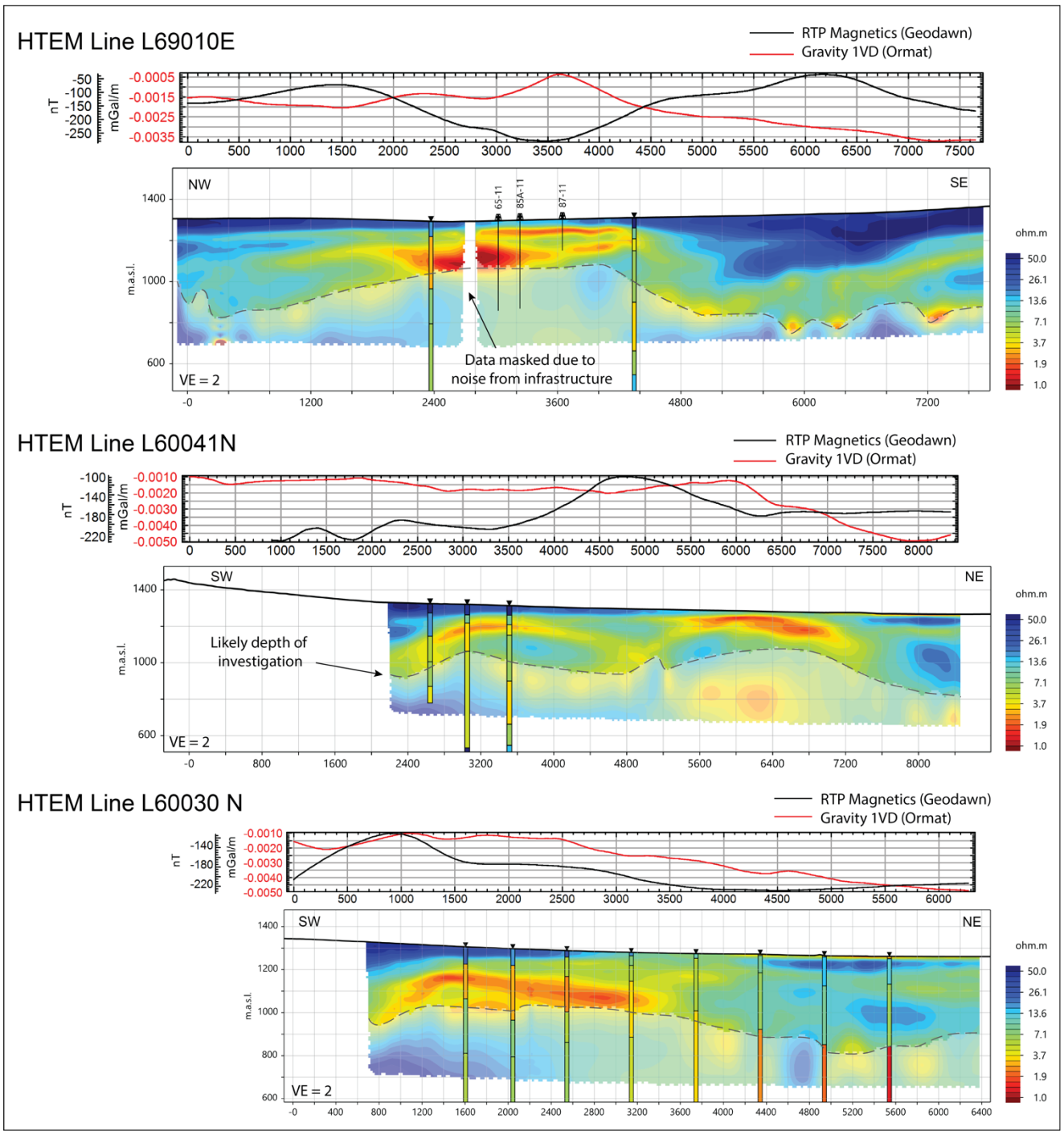

Figure 3: HTEM cross sections discussed in the paper overlain by 1D stick models of the TE model of Ormat's MT data, as well as geophysical profiles: gravity 1VD (Ormat) and Magnetics RTP residual (GeoDAWN) along the HTEM lines. The HTEM likely depth of investigation is shown by a dashed line following the methods of Vest Christiansen & Auken (2012). See Figure 2 for section line locations.

The essential reference for this study has been the general conceptual model for DAC based on Ormat's proprietary data, as presented previously in Delwiche (2013), Orenstein & Delwiche (2014; 2015), Winn et al. (2021; 2023) and Feucht et al. (2024). Elements of the conceptual model are presented in Figure 4 along the BRIDGE HTEM line 69010 E, with inferred natural state isotherms from downhole temperature logs of several wells, and geology from Delwiche (2013). The currently exploited resource at DAC is outflow hosted in Quaternary-Tertiary basin fill sediments (poorly sorted sands, gravel, silt and clay) that are hydrothermally altered (Delwiche, 2013; Orenstein & Delwiche 2014). Inferred upflow to the basin fill sediments is hosted in fracture zones created by the southwest-striking northwest-dipping normal faults penetrating Tertiary ash flow tuffs and andesite and likely Mesozoic meta-sedimentary rocks. Deep exploration drilling indicates that the Tertiary volcanic rocks are relatively low permeability compared to the basin fill sediments, as

evidenced by the linear (conductive) temperature gradient in wells penetrating these rocks. The shallow reservoir consists of fluids at temperatures between ~120 to 130°C (Figure 4).

The interpretation of fluid flow pathways presented in Figure 4 differs from previous models in that we posit an additional shallow outflow near well 87-11 that may or may not be separate from the slightly deeper reservoir hosted in basin fill sediments, as discussed in a subsequent section. The low-resistivity zones observed in the HTEM correspond to relatively closely spaced isotherms, indicating conductive temperature gradients and overall low permeability in these zones. These low-permeability low-resistivity zones visible in the HTEM line appear to overlie the geothermal reservoir, similar to the patterns of low-resistivity hydrothermal smectite observed in many volcanic-hosted geothermal systems worldwide (the "clay cap" model, e.g. Ussher et al., 2000; Cumming, 2016). In order to better characterize the petrologic origins of the low-resistivity zones and the specific geometries and features of the HTEM data, we analyzed core and cuttings from 4 geothermal wells at DAC, the labelled wells in Figure 2, with a subset labelled in Figure 4. The analyses included sample inspection, laboratory infrared reflectance spectroscopy, and methylene blue (MeB) analysis.

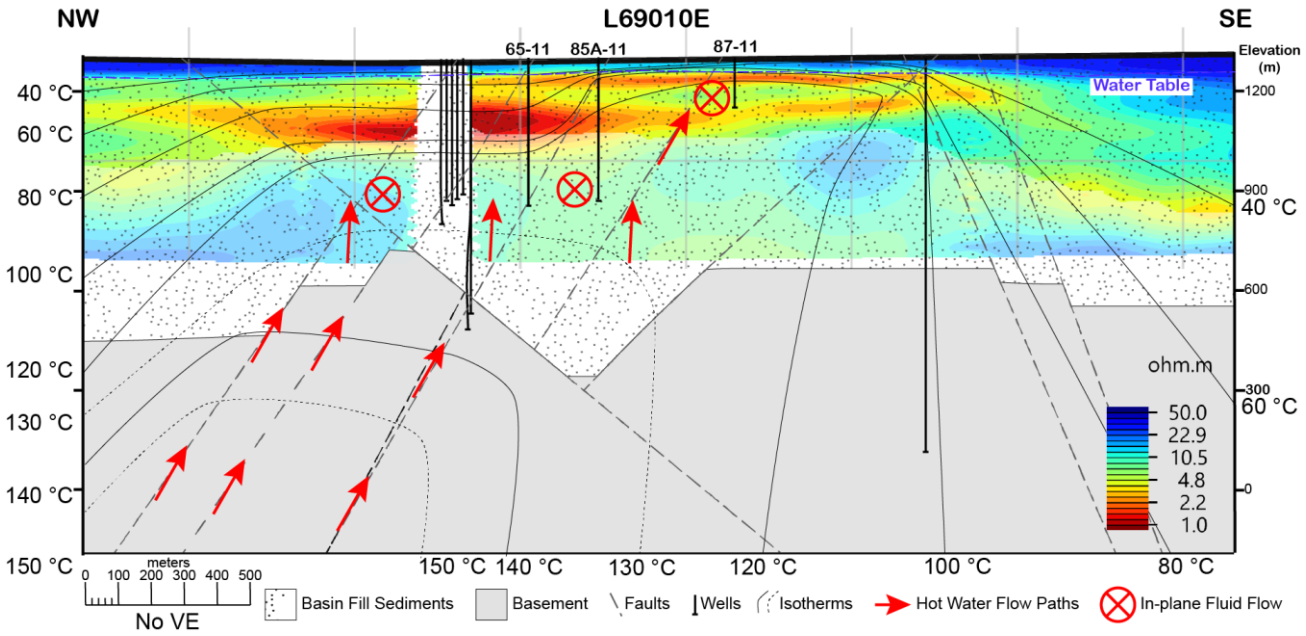

Figure 4: Conceptual model cross-section superimposed on an HTEM resistivity pattern (from line L69010E) with natural state (pre-production) inferred isotherms, hot water flow paths, and simplified geology. The gap in the HTEM profile left of center is due to interference from power plant equipment at the surface. The basement combines both the intersected Tertiary volcanics (ash flow tuffs and andesite) and the inferred Mesozoic rocks beneath.

3. METHODS

3.1 Samples Investigated and Sample Inspection Techniques

Subsurface rock samples from four geothermal wells or boreholes from DAC were investigated (Figures 2 and 4). Two of the wells (87-11, 24-12) had drill core collected (from 0 to 152.4 m total depth), and these cores were viewed, relogged using a binocular microscope, and analyzed using a portable infrared spectrometer at the Great Basin Science Samples and Records Library, operated by the Nevada Bureau of Mines and Geology. The core wells were chosen for analysis because they intersect both the high in the gravity 1VD, and the embedded resistor as observed in the HTEM data (line T69010E). The analyses of the two additional wells, 85A-11 and 65-11, were conducted on drill cuttings collected at ~3 m (10 ft) intervals from surface to 433 m and 443 m depth, respectively. The cuttings samples were washed, dried, and logged on site by the mud loggers. The cuttings were analyzed using the portable infrared spectrometer at the University of Nevada, Reno, and with MeB analysis at Geologica in Reno, NV. These cuttings samples were chosen because they lie along the HTEM line (T69010E) that directly crosscuts the geothermal system and they intersect low resistivity zones. Several cuttings intervals were contaminated with Lost Circulation Materials (LCM) or there were no returns, in which case no analysis was performed. All four wells intersect poorly sorted Quaternary-Tertiary alluvial basin fill sediment of variable grain size and variable hydrothermal alteration mineralogy.

3.2 Laboratory Infrared Reflectance Spectroscopy

The spectrometer used in this study is a Spectral Evolution SR-5400, that measures in the Visible-Near Infrared and Short-Wave Infrared wavelength ranges (from 5 nm to 2500 nm). The instrument's analytical reproducibility is 0.1 nm with a wavelength accuracy from 1 to <3 nm, depending on the wavelength. Measurements were collected using a contact probe that has a field of view of 2 cm in diameter.

Measurements are presented in reflectance relative to a white reference plate. White reference measurements were made at the start of data collection and every 15 to 20 minutes thereafter. For core, measurements were made at approximately 0.6 m increments (2 ft), targeting both representative lithology and hydrothermal alteration and veining. For drill cuttings, each cuttings sample collected at ~3 m (10 ft) was analyzed with a single representative measurement.

Data processing and analysis was performed using a combination of expert driven and statistical approaches. Each spectrum was analyzed individually by an expert spectroscopist and compared to standard mineral reference libraries (e.g. Kokaly et al., 2017). In addition, several supervised classification algorithms were utilized using the material identification tool in the ENVI software package (Version 6.1). The algorithms Spectral Angle Mapper, Euclidean Distance, and Spectral Information Divergence were utilized to aid in the identification. Each spectrum was classified as containing up to three minerals, and the subjective confidence of each classification was recorded on a scale from 1-5, with 1 being low confidence, and 5 being high confidence. In addition to mineral identification, numerical data from the spectra, known as spectral scalars, were calculated from spectra with continuum (hull) removed using a Python script. The continuum removal was performed using a Python script by Hassanzadeh (2020), which uses the approaches by Kokaly & Clark (1999). The spectral scalars utilized in this study are the depth and wavelength position of the 1900 nm absorption feature, associated with H2O, and the 2200 nm feature, associated with the Al-OH bond (Clark et al., 1990; Yang et al., 2011). These are used to calculate the Illite Spectral Maturity (ISM) index to estimate relative abundance of illite:smectite (Pontual et al., 1997; Simpson & Rae, 2018). Table 1 shows the calculations used for the spectral scalars discussed in the text. Simpson and Rae (2018) found that ISM values calculated from hull corrected spectra of less than 0.76 corresponded to smectite, 0.76-96 corresponded to interlayered illite smectite, and >.96 corresponded to illite without smectite based on comparison with XRD analysis. We have accepted these numbers as being sufficiently representative for our initial interpretation, although calibration of the samples from this study through XRD analysis could improve the analysis. The depth (or strength) or absorption features is related to abundance, as well as overall albedo and grain size (Clark et al., 1990). Here, we test the assumption that the depth of the 1900 nm feature (D:1900) is primarily a function of relative abundance, utilizing MeB analysis (Section 3.3).

Table 1: Spectral scalars calculated in this study. All scalars were calculated from continuum removed spectra following Kokaly & Clark (1999). "Dxxxx:yyyy" refers to feature depth of largest feature in wavelength range xxxx to yyyy (nm). "Wuuuu:vvvv" refers to wavelength (nm) of deepest feature within wavelength range uuuu to vvvv.

Scalar Name	Calculation	Description	Source
Illite Spectral Maturity (ISM)	(1-D1800:2020) / (1-D2180:2232)	Measures ratio between Al-OH absorption and H_2O absorption features. It is related to the amount of water in the mineral structure compared to Al-OH, and can be used to estimate relative abundance of illite:smectite. Higher ISM values indicate higher illite or muscovite relative to smectite.	Similar to calculations used by Simpson and Rae, 2018; Pontual et al., 1997
Al-OH Wavelength (W:2200)	W2180:2232	This wavelength is related to illite/muscovite composition and Al-OH mineral structure	Clark et al., 1990; Yang et al., 2011
Depth of H2O feature (D:1900)	D:1800:2020	Strength of H_2O absorption in clay minerals, can approximate relative hydrated clay abundance	Clark et al., 1990

3.3 Methylene-Blue Analysis

Methylene-blue analysis is a quick and inexpensive technique used to analyze drilling muds and applied to estimate smectite content of geothermal well cuttings at the well site during drilling (Gunderson et al., 2000). The Methylene Blue (MeB) test for estimating swelling clay content utilized in this study are those of Harvey (1993) updated and annotated by Cumming (2004, 2010, 2015, 2020). One gram of each sample was ground to a consistent grain size using a coffee grinder and added to a flask with 25 ml of water and 1 ml of dilute sulfuric acid (5N). The solution was then boiled gently for 2 minutes. Following boiling, 3.74 g/l MeB solution was added at 0.5 mL increments, until the maximum amount of MeB was absorbed by the clay (as described by Harvey, 1993). The MeB solution utilized was calibrated with commercial bentonite of 60 to 70% smectite and was found to be within that range (64%), therefore 1 mL of MeB is approximately 1% smectite. Further analysis, such as comparison with clay fraction X-Ray Diffraction (XRD) analysis could better constrain the percent smectite, however time and budget constraints prevented XRD validation and calibration for this project.

4. RESULTS

4.1 Mineral Identification

The following minerals were identified using infrared spectroscopy: smectite, illite, kaolinite, calcite, opal, with rare chlorite, hematite, and zeolites (Figure 5). Smectite is by far the most common mineral detected in the wells and is characterized by strong absorption features at 1400, 1900, and 2210 nm (Figure 5A, Kokaly et al., 2017). Illite is also common in the wells, and is characterized by absorption features at 1400, 1900, 2200, and 2350 nm (Figure 5A, Kokaly et al., 2017). It is found alongside smectite, and our interpretation is that it is primarily present as interlayered illite smectite, although smectite overprinting illite could produce a similar spectral signature. Kaolinite, characterized by a distinct doublet absorption feature near 2200 nm, is uncommon in the well, and typically found at less than 50 m depth

in wells 87-11 and 24-12 (Figure 5B). Opal and chalcedony, characterized by a wide absorption feature near 2200 nm were also identified (Figure 5D). In the deeper sections of the wells, a mixture of smectite, illite, calcite, and opal/chalcedony is very common (Figure 5C) and is difficult to unmix for high confidence mineral identification. Follow-up XRD analysis on these samples could help better understand this mixture. In addition, an unknown mineral(s) was found in several samples from well 24-12 that had additional absorptions near 1400 nm, similar to sulfate minerals such as gypsum, alunite, and jarosite, however a match with existing library minerals was not found.

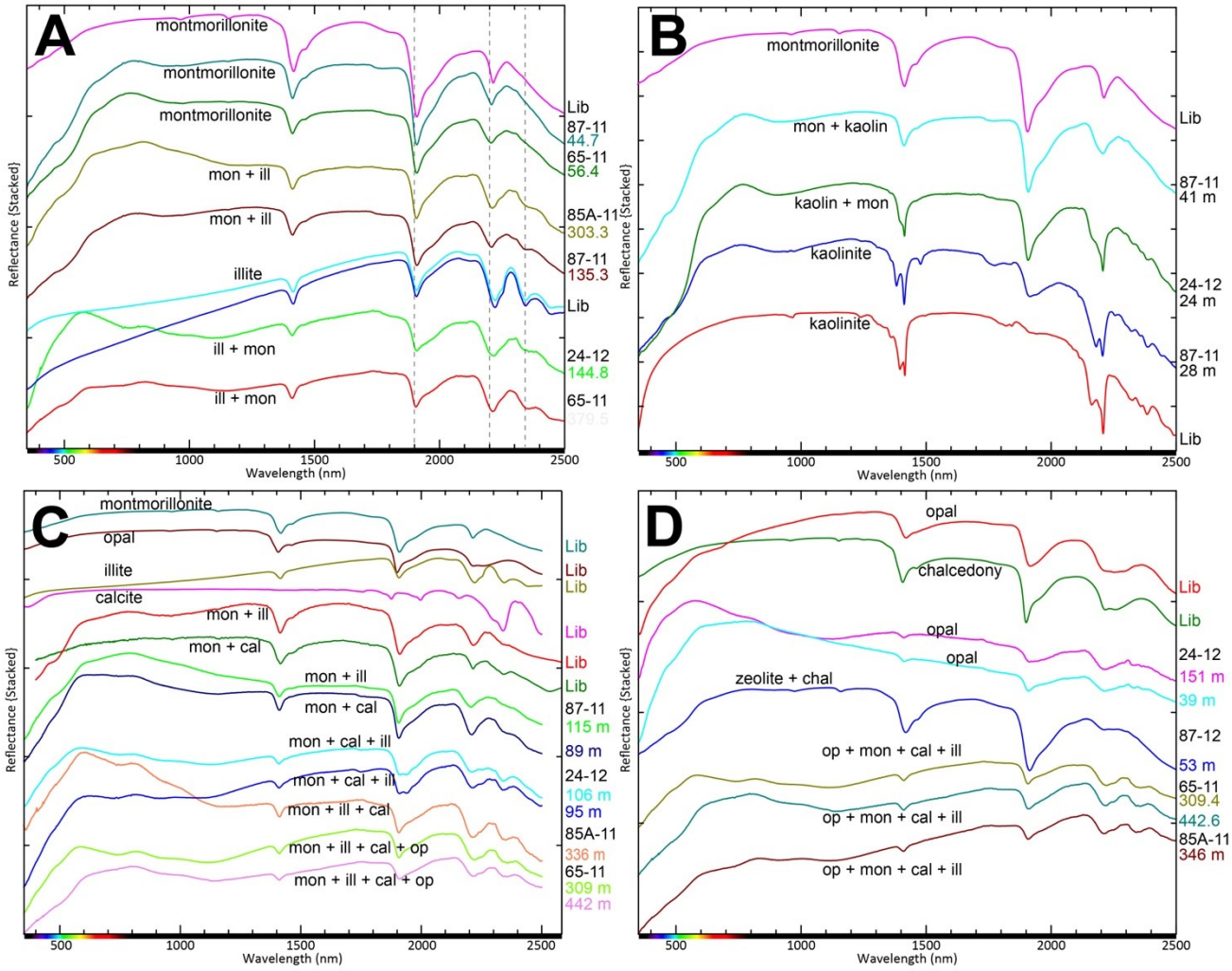

Figure 5: Representative spectra from DAC wells alongside library minerals from Kokaly et al., (2017). A: Smectite (montmorillonite) and illite, B: Kaolinite and smectite, C: Common mixtures observed (montmorillonite + opal + illite + calcite), D: Silica polymorphs (opal and chalcedony) and common mixtures measured containing opal. Side annotation: Lib refers to library mineral, and each measured spectrum is labeled with well name and depth.

The following secondary minerals were identified through sample inspection: clay, quartz and other silica polymorphs, pyrite, calcite, and hematite (e.g. Figure 6). Swelling clays are observed throughout the unconsolidated sediments, with obvious swelling following wetting of the core samples during inspection. Silica is primarily found cementing sand and gravel clasts (Figure 6A), or as less common drusy quartz infilling cavities (Figure 6C). Silica veining was found to be rare-absent in the shallower core wells investigated, however it is uncertain if the deeper wells with drill cuttings samples also lack silica veining. Pyrite at DAC is found most often associated with silicification (Figure 6D). Massive and microcrystalline calcite (Figure 6B) is observed cementing sand and gravel clasts. Hematite, and rare Goethite are observed most often in clay-rich sections of the wells. Unknown/unidentified fibrous zeolite (?) minerals are also present.

4.2 MeB Analysis and SWIR Calibration

Table 2 shows the results of 14 MeB analyses on cuttings from wells 85A-11, and 65-11. Computed smectite amounts in the samples ranged from 1 to 13%. A linear correlation was observed between the MeB analysis and several of the spectral scalars (D:1900 and ISM; R2 values of 0.9585 and 0.8644 respectively). These linear trends were utilized to calibrate a conversion equation to estimate percent of smectite (or ml of MeB) from the spectral scalars alone. Here, we present the average percent smectite between the two calibrations for each SWIR measurement (Figure 8-10).

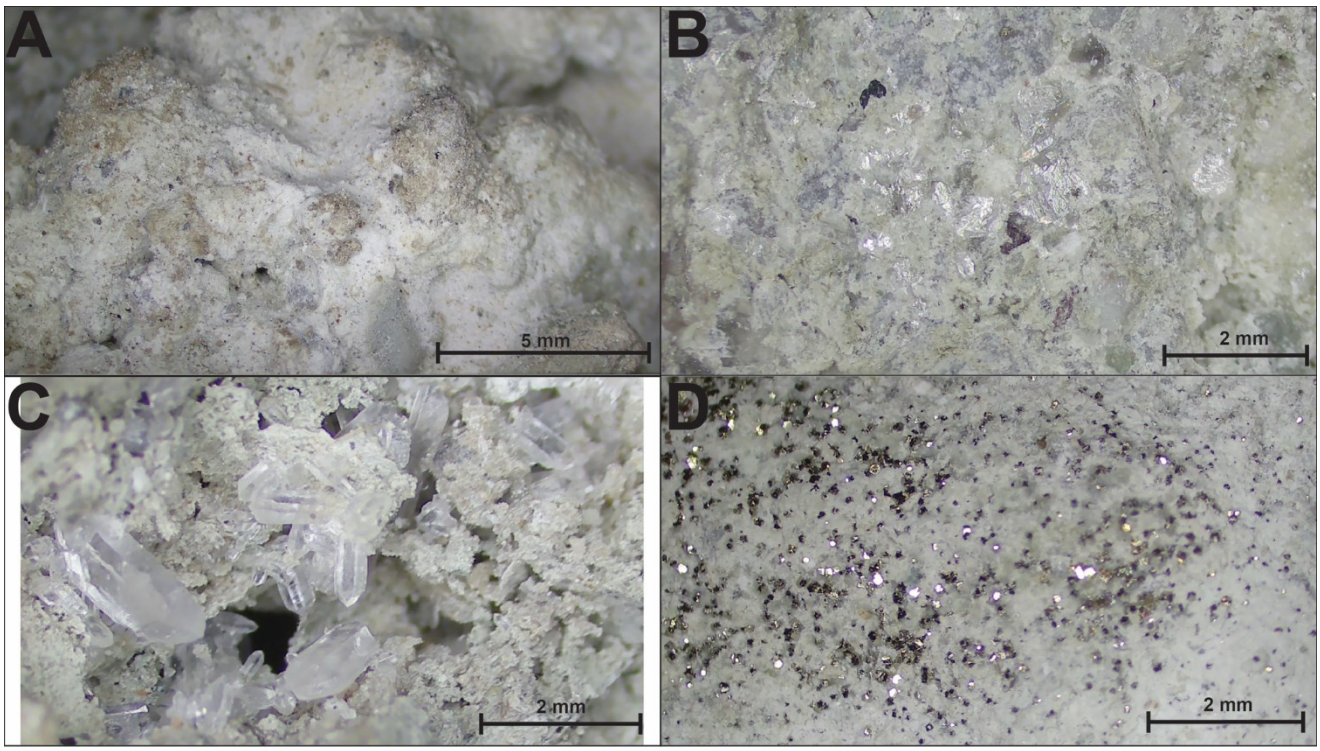

Figure 6: Example microscope images of common hydrothermal alteration minerals visible in core from DAC. A: Massive silica cementing (white) between sand grains from well 24-12, depth 372 ft, B: Massive calcite cementing from well 24-12, depth 423 ft, C: Drusy quartz in open space from well 24-12, depth 427 ft, D: Abundant pyrite accompanied by massive silica cementing observed in well 24-12, depth 387 ft.

Table 2: Results of MeB analysis, with spectral scalars ISM and D:1900 for reference. Each drop represents 0.5 mL of MeB solution.

SAMPLE NAME	Drop Count	Sample mass (g)	Solution Concentration (M)	Solution Amount (ml)	Smectite % Computed	ISM	D:1900
85A-11_200	11	1	0.096154	26	5.5	0.69	0.37
85A-11_230	17	1	0.096154	26	8.5	0.68	0.40
85A-11_300	10	1	0.096154	26	5	0.76	0.30
85A-11_480	9	1	0.096154	26	4.5	0.75	0.32
85A-11_610	16	1	0.096154	26	8	0.69	0.38
85A-11_750	13	1	0.096154	26	6.5	0.70	0.36
85A-11_910	12	1	0.096154	26	6	0.74	0.32
85A-11_1100	3	1	0.096154	26	1.5	0.94	0.09
85A-11_1370	2	1	0.096154	26	1	0.92	0.12
65-11_310	11	1	0.096154	26	5.5	0.71	0.34
65-11_510	18	1	0.096154	26	9	0.63	0.45
65-11_650	26	1	0.096154	26	13	0.58	0.49
65-11_980	7	1	0.096154	26	3.5	0.88	0.17
65-11_1230	6	1	0.096154	26	3	0.81	0.23

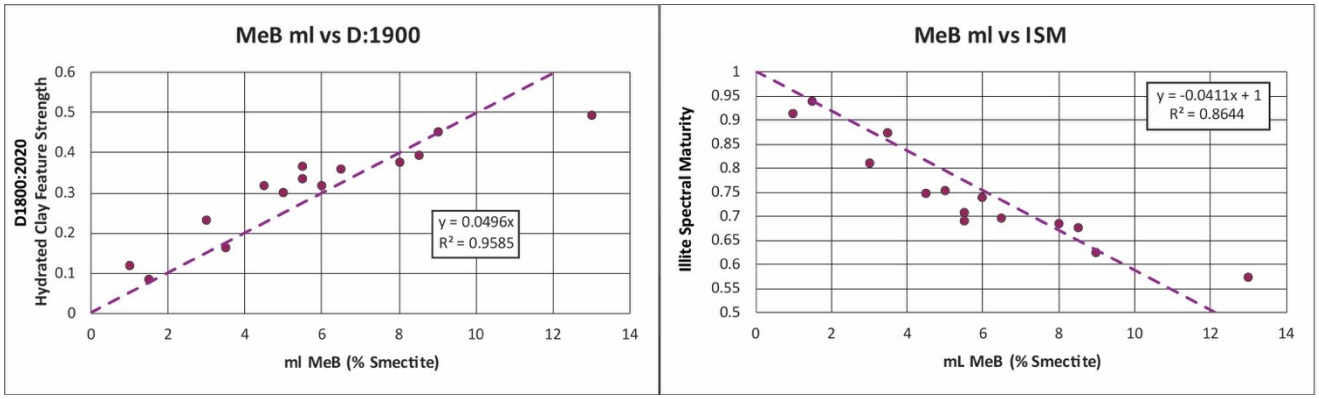

Figure 7: Methylene-blue (MeB) analysis versus spectral scalars (D:1900 and Illite Spectral Maturity, ISM) with linear regression results (set intercept of 0 and 1 respectively) used for the smectite abundance calibration.

4.3 Comparison with other downhole data and geophysics

Figures 8 to 10 show the results of the SWIR mineral analysis, MeB analysis, and sample inspection for the four wells investigated, as well as the temperature logs, and the extracted resistivity from the closest HTEM line (L69010E). The distance of the wells from the HTEM line varies from 22 to 709 m, as noted in the figure caption.

For well 85A-11 (Figure 8) and well 65-11 (Figure 9), SWIR analyses of cuttings identified a general zonation of smectite, predominantly from 0 to 275 m depth, changing to interlayered illite-smectite, calcite, and silica polymorphs with rare chlorite from 275 m to total depth (~440 m). This general pattern is consistent with the spectral scalars (ISM & D:1900) and the measured and calculated percent smectite based on the MeB analysis. The shallower interval (0-275 m) has higher smectite content (between 5 and 12%), higher hydrated clay feature strength, and lower illite spectral maturity (<0.8) than the deeper interval (275-440 m), characterized by lower smectite content (between 0.5 and 5%), lower hydrated clay feature strength, and higher illite spectral maturity (between 0.8 and 1) consistent with interlayered illite-smectite. This mineralogical transition at 275 m depth is also observed in the temperature data from the wells, with a change to near isothermal temperatures of 128°C at ~300 m, indicative of a permeable reservoir.

Interpretation of spectral scalars and the calculated percent smectite from the MeB analysis and calibration identify additional subzones than those described above, that are consistent with the resistivity from the HTEM data. From shallow to deep in well 85A-11 (Figure 8), there is: relatively high smectite (between 6 and 8%) from 25 to 75 m depth, which corresponds to relatively low resistivity (2.17 ohm.m) centered around 57 m depth; relatively low smectite (~4-6%) between 75 and 150 m corresponding to relatively high resistivity (4.56 ohm.m) at 110 m; relatively high smectite (between ~7 and 8%) from 150 to 300 m corresponding to relatively low resistivity (2.45 ohm.m) at 175 m; and finally relatively low smectite (between 0.5 to 3%) from 300 to 440 m corresponding to relatively high resistivity values of ~7.75 ohm.m. For well 65-11: estimated smectite abundance of between 4 and 8% from 40 to 140 m corresponds to resistivity values of between 2.37 and 3.92 ohm.m; relatively high smectite (between 8 and 13%) from 140 to 275 m corresponds to relatively low resistivity (1.27 ohm.m) at 175 m, and finally relatively low smectite (between 1 and 4%) at depths from 275 to 440 m corresponds to relatively high resistivity (between ~7 and 8.2 ohm.m).

For wells 87-11 (Figure 10) and 24-12 (Figure 11), SWIR analysis of core identified a zonation of smectite with rare kaolinite from ~0 to 70 m, with increasing interlayered illite-smectite, calcite, and opal to TD at ~150 m. This transition in SWIR identified minerals at ~70 m corresponds with as shift from a conductive temperature gradient profile to a near isothermal gradient at ~128°C. For well 87-11, several distinct hydrothermal alteration zones are apparent based on SWIR mineral analysis, SWIR spectral scalars, and sample inspection (Figure 10). Zone 1, from 0 to 45 m depth, has ~6% smectite, minor kaolinite, and calcite, a conductive temperature gradient, and a transition in resistivity from shallow high values (~15.5 ohm.m) to moderate values (~3.5 ohm.m). Zone 2, from 45 to 70 m, is characterized by high smectite values (between 6 and 12%), minor silica, calcite, and hematite, a conductive temperature gradient, and a resistivity low of 2.04 ohm.m at ~ 50 m depth. Zone 3, from ~70 to 130 m, is characterized by relatively low estimated smectite (between 2 and 6%), interlayered illite smectite, abundant opal and other silica polymorphs, abundant pyrite, calcite, near isothermal temperature gradients, and local high in resistivity of 5.7 ohm.m. Zone 4, from ~130 to 150 m, is characterized by slightly higher estimated smectite than Zone 3 (between 6 and 10%), more common calcite relative to silica, and slight decrease in resistivity to ~ 4 ohm.m at 150 m depth. Well 24-12 varies significantly from well 87-11, with less distinct zonation in secondary minerals, and overall lower grainsize of the host rock. In general, there is relatively high estimated smectite content (between 4 and 10%) from 0 to 60 m depth, with a general decrease in smectite from 60 to 150 m, and generally increasing silica, pyrite, and calcite with depth. In addition, an unknown sulfate mineral is present throughout the well, here plotted as “gypsum”. There is less agreement between the smectite zonation and the HTEM resistivity in this well, and this could be because the well is significantly offset from the HTEM line (709 m) compared to the other wells.

Compared to the cuttings samples analyzed, the number of unique minerals identified is higher in the core wells, and there is more noise in the spectral scalar data overall. This is likely because the cuttings samples become relatively homogenized due to mixing during transport up the wellbore, and with possible contamination from shallower portions of the well. This could lead to less unique mineral identifications in cuttings than from the core due to missing less common minerals in the cuttings and the blurring of zone distinctions. A similar pattern is observed between cuttings and sidewall core collected from one well at the Fallon FORGE EGS site (Kraal &

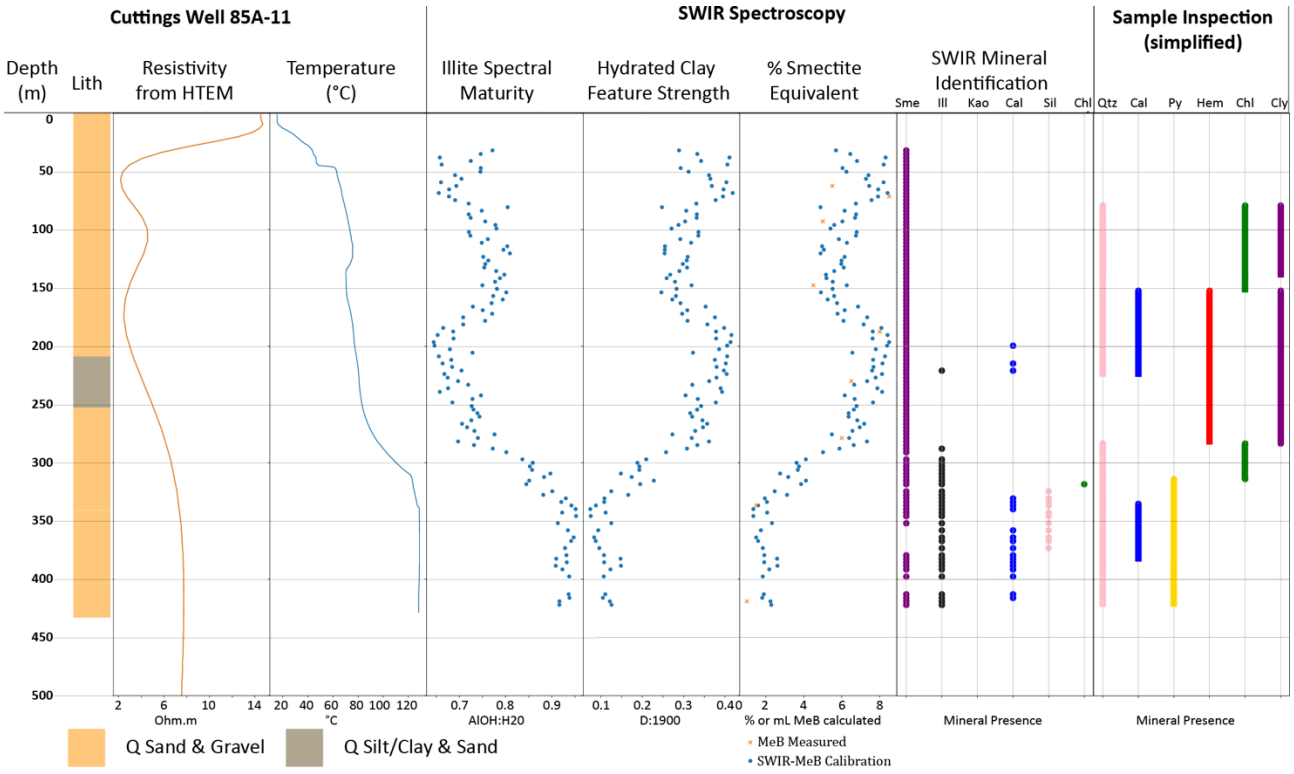

Figure 8: Downhole well logs from well 85A-11, including lithology, resistivity from closest HTEM line, temperature, and SWIR spectroscopy analysis. The projected HTEM line is 294 m from the well. Sme refers to Smectite, Ill refers to Illite, Kao refers to Kaolin group minerals, Sil refers to Silica (Opal, Chalcedony, Quartz), Chl refers to Chlorite, Cal refers to Calcite, Py refers to Pyrite, Hem refers to Hematite, and Cly refers to Clay. Q refers to Quaternary-Tertiary.

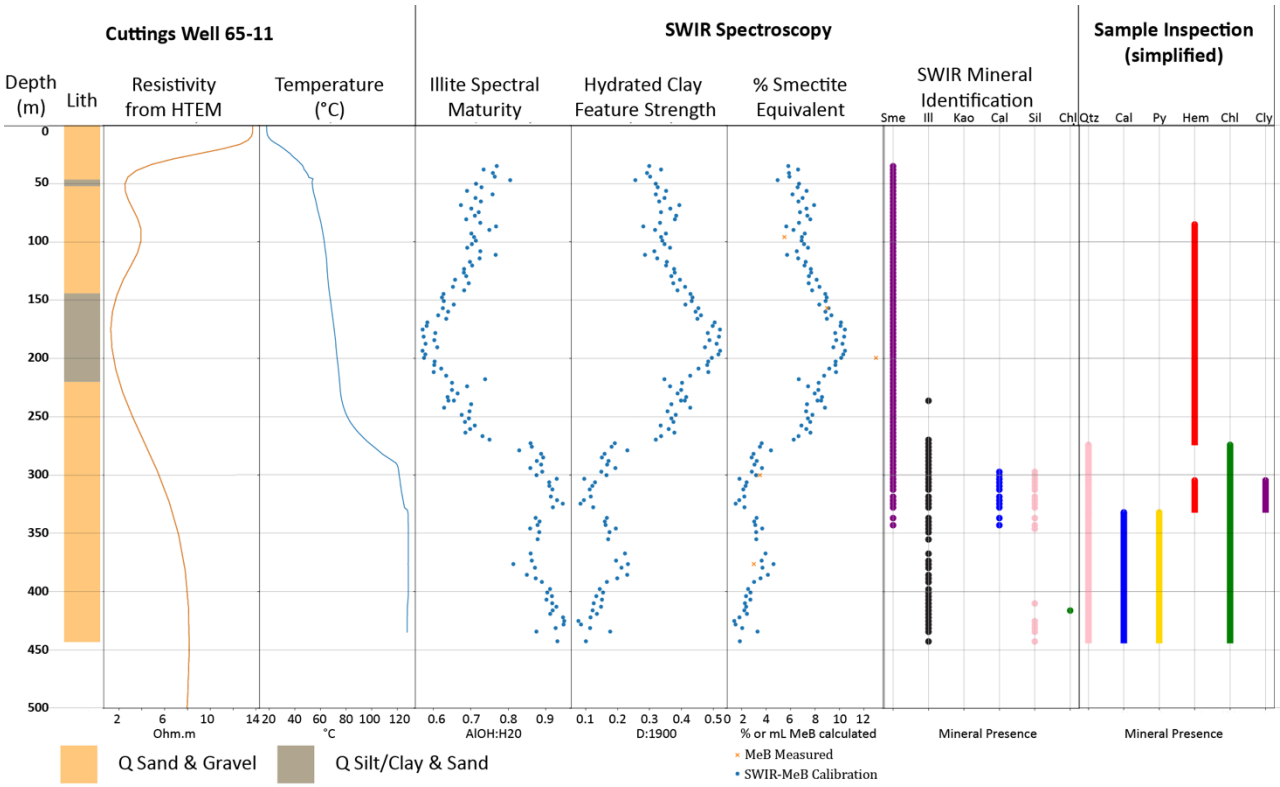

Figure 9: Downhole well logs from well 65-11, including lithology, resistivity from closest HTEM line, temperature, and SWIR spectroscopy analysis. The projected HTEM line is 103 m from the well. Refer to Figure 8 for mineral legend.

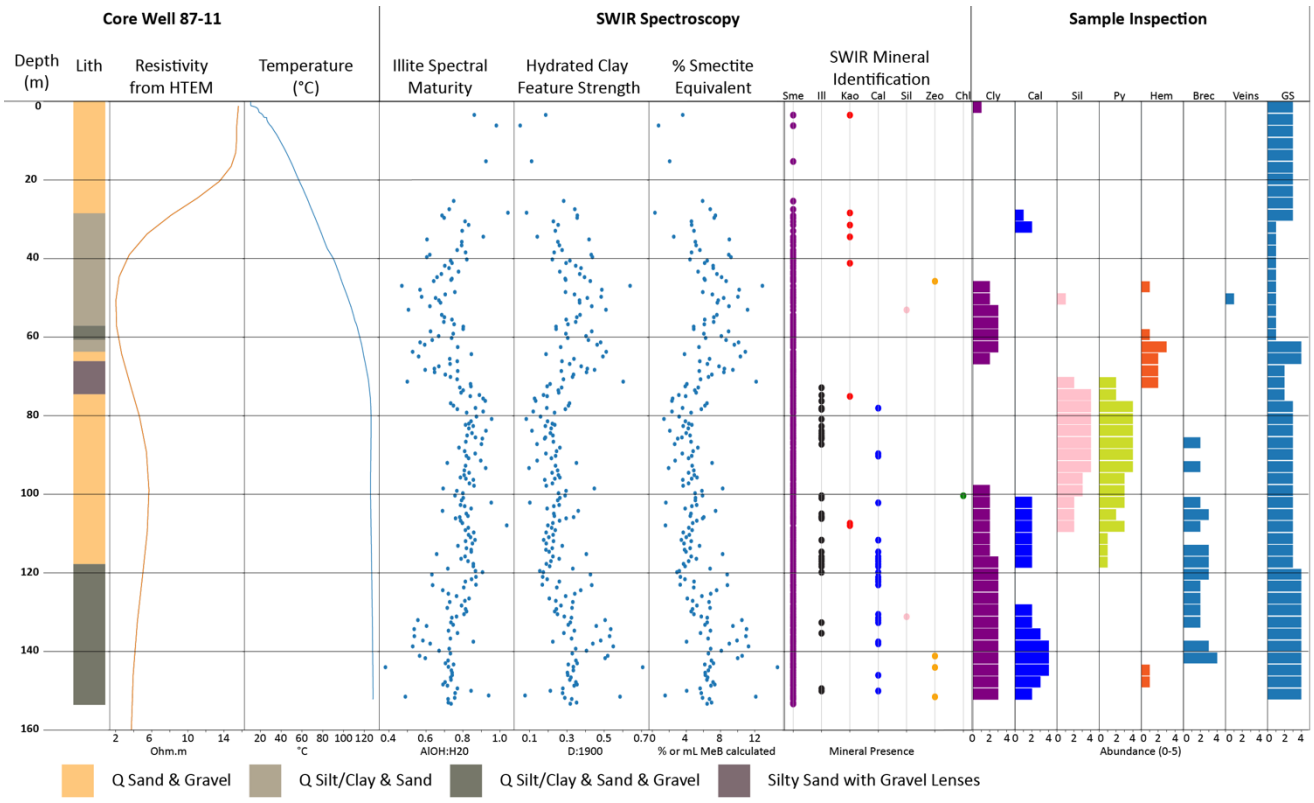

Figure 10: Downhole well logs from well 87-11, including lithology, resistivity from closest HTEM line, temperature, SWIR spectroscopy analysis, and secondary minerals, brecciation, veins, and overall grainsize observed. The projected HTEM line is 22 m from the well. Zeo refers to Zeolite, Brec refers to relative amount of fracturing due to tectonic brecciation, and GS refers to relative average grain size, refer to Figure 8 for additional abbreviations.

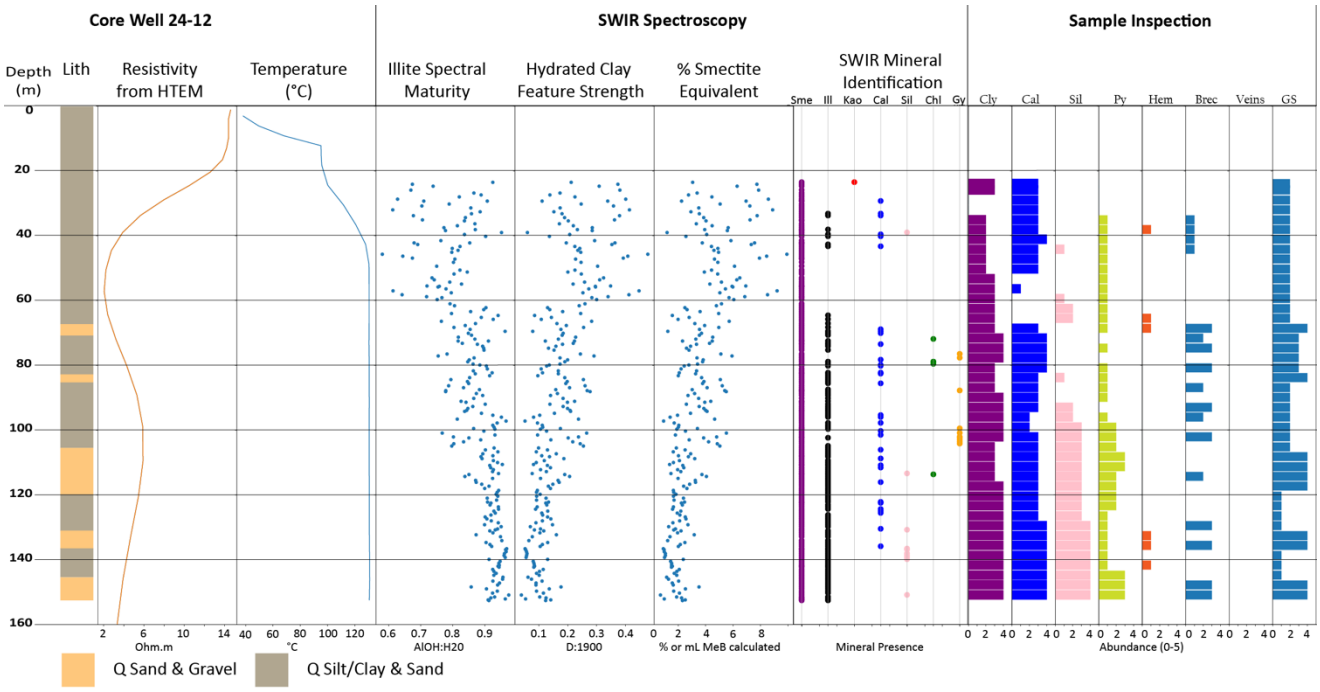

Figure 11: Downhole well logs from well 24-12, including lithology, resistivity from closest HTEM line, temperature, SWIR spectroscopy analysis, and secondary minerals, brecciation, veins, and overall grainsize observed. The projected HTEM line is 709 m from the well. Gy refers to Gypsum (or unknown sulfate mineral, see text for details). Refer to Figure 10 for additional abbreviations.

Ayling, 2019; Kraal et al., 2021). It is also possible that there could be mineralogical differences between the cuttings and core wells, due to intersecting different lithologies and/or hydrothermal alteration zones. This would be consistent with the geophysics and conceptual model, where the core wells intersect a high in the gravity 1VD, inferred to be caused by shallow hydrothermal alteration processes (precipitation of dense secondary minerals in shallow basin-fill sediments).

5. DISCUSSION

5.1 Genetic model of hydrothermal mineral formation at DAC, resulting geophysical signature, and conceptual model.

As discussed in section 3.3, there is a prominent relationship between resistivity as observed in the HTEM line(s) and the smectite content of the wells that intersect the line, and also with the secondary minerals observed, such as silica, calcite, and pyrite. Our interpretation is that these minerals are present due to hydrothermal alteration of the basin fill sediments by the geothermal fluids. Smectite is a typical hydrothermal alteration product of neutral pH hydrothermal fluids at less than 180°C (Browne, 1978; Henley & Ellis, 1983; Reyes, 1990). Interlayered illite-smectite is most common at higher temperatures in volcanic environments (180-225°C). These mixed layers are often present at lower temperatures down to ~150°C, although smectite is usually more predominant, and it is uncertain if they are in equilibrium. The typical temperature range for interlayered illite-smectite is higher than currently observed at Don A Campbell (~130°C max temperatures in basin fill sediments). There are several possible interpretations for the presence of illite: A) the system was hotter in the past, and the interlayered illite-smectite is a relict mineral from this previous hotter period, B) interlayered illite-smectite stability might occur at lower temperatures when hosted in basin fill sediments, C) the illite was present in the primary rock and is not a product of hydrothermal alteration, or D) the current interpretation of the SWIR mineralogy incorrectly identified a mixture of smectite, calcite, and silica as also containing illite. We will discuss the four possibilities below, emphasizing our preferred interpretation, a combination of scenarios A and B.

Based on the evidence from the DAC reservoir and other geothermal systems, it is more likely than not that the DAC system has been hotter in the past. Relict high temperature alteration minerals have been observed at most geothermal fields where detailed hydrothermal mineral characterization has taken place, such as those in volcanic environments of the Philippines, New Zealand, and the Geysers, USA (e.g. Reyes, 1990; Chambefort et al., 2017; Walters et al., 1991; Moore et al., 2000) as well as in deep-circulation type systems in the U.S. Great Basin at Desert Peak (Lutz et al., 2009), and the Tungsten Mountain geothermal field (Kraal, 2023). It appears that many hydrothermal systems display cyclical qualities, with initial vigorous activity and slow decline in both temperature and permeability, often followed by reinvigoration (e.g. Lutz et al., 2002). Mechanisms for temperature decline are exhaustion of heat source (e.g. from the magma body in volcanic hosted systems), decline in permeability (often due to precipitation of vein filling minerals (e.g. Rimstidt & Barnes, 1980; Fournier, 1989; Sibson, 1987; Elders et al., 1979), and cold water influx leading to collapse of the system. Mechanisms for reinvigoration are intrusion of new magma bodies providing heat (for volcanic hosted systems), and creation/maintenance of new fracture permeability through faulting and earthquake activity (e.g. Sibson, 1987; 2000; Siler et al., 2023). A lowering of the water table such as those due to climatic factors, fault-driven uplift, or valley incision could also lead to the overprinting of deeper (higher-temperature) alteration minerals by shallower (low-temperature) minerals (e.g. Sillitoe 2015).

Temperature stability ranges commonly used for interpretation of geothermal minerals, such as those referenced above (e.g. Browne, 1978; Henley & Ellis, 1983; and Reyes 1990) are based primarily from empirical studies of active geothermal systems in high temperature volcanic environments, and to a lesser extent based on laboratory water-rock interaction experiments and numerical modeling. It is possible that further work analyzing hydrothermal alteration mineral zonation in low-moderate temperature geothermal systems may find different temperature ranges than those conducted in high temperature environments due to variability in fluid and rock chemical composition between these end members.

It is possible that variability in the basin-fill sediment provenance may play a role in the resistivity structure and smectite content observed. For example, low resistivity zones similar to the pattern at DAC are sometimes associated with mudstones from former lakes. However, the low resistivity zone corresponding to high smectite content at DAC appears to be directly co-located with the extent of the active geothermal system, and therefore it seems likely that former is a product of the latter. Petrographic analysis, such as described by Stimac (2023) through observation under polarized light, and/or utilizing Scanning Electron Microscopy could better elucidate the origin of the hydrothermal alteration minerals and their paragenesis, and provide more information about the original sediment sources. However, it is also likely that sediment grain size and composition can play a role in shallow hydrothermal fluid flow, where coarser grained high permeability units (e.g. fanglomerates, beach deposits) provide shallow fluid flow pathways, and fine-grained deposits (such as lake sediments) provide caps and lateral barriers. Moreover, hydrothermal alteration processes could further modify the permeability and porosity of these sediment end members through the precipitation of secondary minerals.

Lastly, because it is possible that there is a mineral mixture misidentification a follow-up XRD study on the clay sized fraction of the cuttings analyzed could further confirm our interpretation of the SWIR data. However, best practices were utilized for high precision identification of minerals using laboratory SWIR spectroscopy, including statistical methodologies for spectra matching, as well as visual confirmation of each match by a spectroscopist. Previous work by the authors (Kraal et al., 2021; 2023a; 2023b) and others (e.g. Calvin and Pace, 2016; Simpson and Rae, 2018) find general agreement between SWIR mineral identifications and other methods such as petrographic microscopy and XRD.

In addition to the contributions of smectite and illite-smectite to the geophysical signature of the site, including resistivity and density, the precipitation of silica polymorphs, calcite, and pyrite also have an effect. The near surface embedded resistor and the near surface densification inferred from the gravity 1VD could be the product of the precipitation of silica and calcite. Silica polymorphs (opal, chalcedony, quartz) are common alteration products from a cooling silica saturated fluid (Fournier, 1985a). Calcite, with reverse solubility, can either be precipitated from a cooling geothermal fluid when boiling, or through heating of cold CO2-rich groundwater at the margins

of the system (Fournier, 1985b). Both minerals would increase the density of the basin fill sediments, and raise the resistivity by reducing the porosity (hydration) of the smectite. Pyrite is a common secondary mineral ubiquitous to geothermal systems with a wide temperature stability range (Browne, 1978; Henley & Ellis, 1983; and Reyes 1990). Pyrite is found at DAC in highest abundance alongside silicification. Hematite is often formed in hydrothermal environments through oxidation of secondary pyrite, sometimes near the water table in the steam heated zone (Sillitoe, 2015). At DAC, hematite is most abundant in the shallow portions of wells associated with areas of high smectite concentration, possibly formed through the oxidation of pyrite.

Figure 12 is a conceptual model diagram focusing on the outflow part of the system along the HTEM line L69010E based on our interpretation of the well data, and geophysical results, showing several hydrothermal alteration mineral zones hosted in the basin fill sediments. The main hydrothermal alteration zones are as follows: 1) a thin kaolinite + smectite + hematite zone with minor calcite above the argillic zone at and near the current water table, potentially formed from steam-heated advanced argillic overprinting of smectite above the shallow outflow reservoir hosted in the embedded silicified zone. 2) an argillic zone composed of abundant smectite (5-13-% based on MeB analysis) commonly found with hematite, resistivity values of less than 3 ohm.m, and generally conductive temperature gradients (inferred from closely spaced isotherms) due to overall low permeability (the clay cap); 3) a shallow silicified and calcified zone characterized by lower smectite content (2-5%) likely present as interlayered illite-smectite, found alongside abundant pyrite, and likely relatively high permeability inferred from near-isothermal temperature profiles through this zone, interpreted to correspond to a shallow outflow zone; 4) a larger deeper silicified zone, with silica alteration most abundant along northwest-dipping normal faults, with abundant pyrite, calcite, and lesser interlayered illite-smectite (smectite <2%), and chlorite with overall high permeability as inferred by the frequent mudlosses in these intervals, and the target for production and injection wells in the field. Normal faults within the basin-fill sediments are inferred to provide additional fracture permeability and flow pathways for the hydrothermal fluids, perhaps providing a pathway through the argillic "clay cap" from the deeper silicified zone to the shallow silicified zone (Figure 12). The shallow outflow zone may follow existing higher-permeability sediments, or fracture permeability due to faulting, respectively supported by the presence of coarser sediments in this zone (Figure 10), and normal faulting adjacent to the shallow core wells (Figure 2).

While wells through the shallow outflow zone inferred within the embedded resistor remain isothermal and do not have temperature reversals as commonly occurs below a shallow outflow, outflow is plausible based on the following observations: the embedded resistor is where near-boiling fluids come closest to the water table, it has unique alteration as detailed in this study, and it is in a relatively permeable horizon. If the deeper low resistivity zone is less permeable, and as it is sandwiched between two hot outflow zones, it will come into equilibrium with them and therefore we would not expect a thermal overturn associated with it. Although the outflow direction is uncertain based on the data reviewed here, the northeast flow direction shown in Figure 12 is based on the geometry of the shallow temperature anomaly, the northeast trending high in the gravity 1VD data, and the presence of thermal overturns in wells to the northeast of the study area (Figure 2).

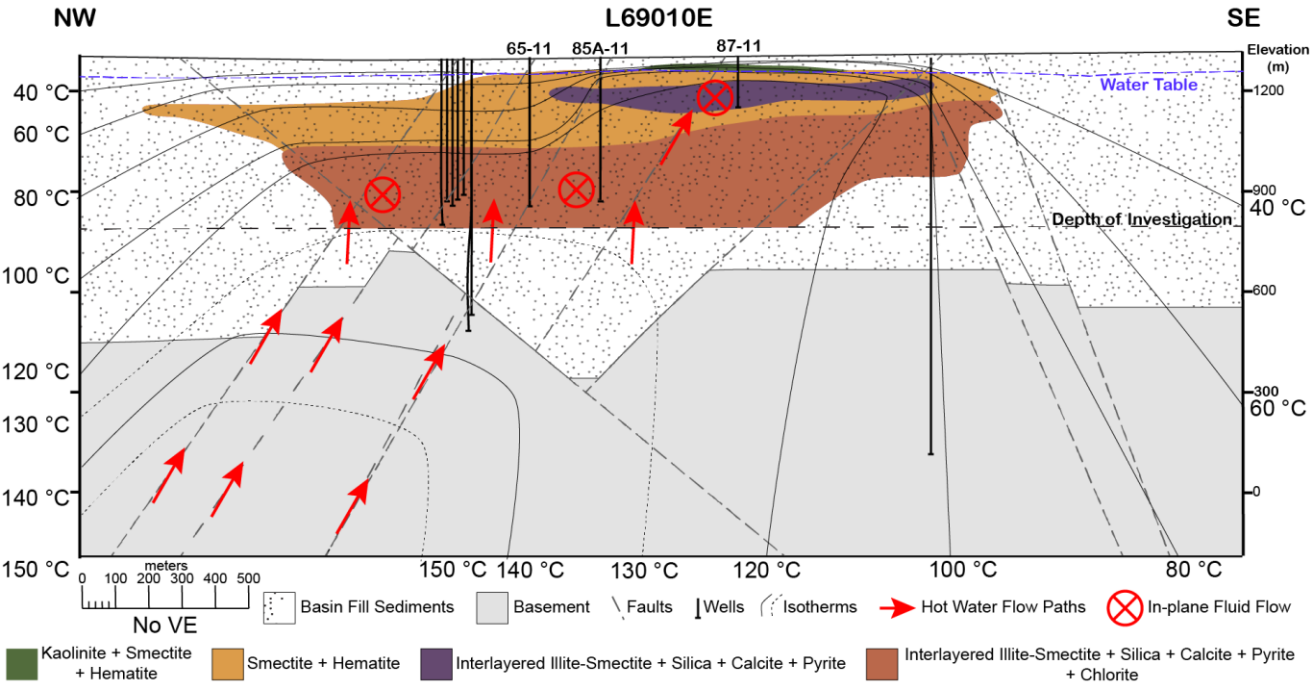

Figure 12: Conceptual model of DAC focusing on characterizing alteration zones hosted in basin fill sediments within and around outflow inferred from well mineral analysis and interpretation of HTEM resistivity data (Figure 3). Zonation below ~800 m elevation (labelled "Depth of Investigation") was not characterized in this study.

5.2 Comparison with other geothermal fields in the basin and range, implications for exploration, and generalized conceptual model.

The DAC geothermal system has many analogues in the Great Basin region, as well as in western Turkey where deep-circulation type systems predominate. DAC is a blind geothermal system, as is expected for most of the undiscovered geothermal resources in the Great Basin (Downs et al., 2025). Even those geothermal developments where most production is from the upflow must have an outflow that dissipates heat, with large hidden upflows requiring a particularly large outflow. Therefore, our interpretation of the relationship between geophysical patterns and hydrothermal alteration mineralogy zonation of the outflow part of the DAC system can be applied to many of the most promising geothermal prospects in the Great Basin. Based on the lack of counterexamples and making reasonable assumptions about cases for which data was not available, it is likely that a shallow low-resistivity smectite zone caps nearly every developed geothermal reservoir in the Great Basin region, as has been observed as the prospects of East Hawthorne, Lee-Allen, Grover Point, Southeast Gabbs, and developed fields like Desert Peak, San Emidio, Tungsten Mountain, Steamboat and Salt Wells (e.g. Sewell et al., 2023; Craig et al., 2021; Folsom et al., 2020; 2023; 2024; Kraal, 2023a; Feucht et al., 2023; Downs et al., 2025). This study provides the petrophysical background needed to interpret details of the resistivity and gravity data sets. Based on these results at DAC and the less detailed but comparable results from San Emidio, the outflow of a geothermal system can be imaged by HTEM or MT as a resistive silicified zone embedded in a shallow low-resistivity smectite zone, a pattern that has also been observed at the Grover Point and Lee-Allen geothermal prospects (Downs et al., 2025). DAC is hosted in displacement transfer zones between kinematically linked strike-slip and normal faults, a pattern analogous to Blue Mountain (Fercho et al., 2023), and Wabuska (Faulds et al., 2021) in Nevada. Undeveloped geothermal prospects in Nevada that have been interpreted to be located in potentially analogous displacement transfer zones include East Hawthorne, Southeast Gabbs, and Lee-Allen, lending structural support to the petrologically informed HTEM resistivity interpretation Lee Allen. These results have been integrated with geochemistry, temperature and hydrological data at Lee Allen in a geothermal resource conceptual model used to justify temperature gradient or slim hole well targets (Downs et al., 2025).

6. CONCLUSION

Shallow low resistivity zones are commonly observed in the basins of the Basin and Range region, some of which are related to clays in lake beds, some to geothermal smectite clay alteration and some to both. When interpreted in the context of petrology, hydrology, structure, and thermodynamics, regional resistivity techniques such as HTEM can be decisive in greenfield geothermal exploration. This work shows that low-resistivity (~ 1-5 ohm.m) zones at the DAC geothermal field are co-located with abundant smectite (5-13%) associated with the low permeability cap over the reservoir. The intermediate (~5-10 ohm.m) resistivity zones are co-located with silicification or calcification associated with the permeable outflow, or with interlayered illite-smectite clays rather than pure smectite. Further petrologic work, such as XRD, thin section petrography, SEM analysis, and Raman Spectroscopy could further validate our interpretation, and provide context and petrogenesis information for the minerals identified in this study.

ACKNOWLEDGMENTS

This material was based upon work supported by the U.S. Department of Energy, Office of Energy Efficiency and Renewable Energy (EERE), Office of Technology Development, Geothermal Technologies Office under the FY2020 Hydrothermal and Low Temperature Multi-Topic Funding Opportunity Announcement DE-FOA-0002219. Sandia National Laboratories is a multi-mission laboratory managed and operated by National Technology & Engineering Solutions of Sandia, LLC, a wholly owned subsidiary of Honeywell International Inc., for the U.S. Department of Energy's National Nuclear Security Administration under contract DENA0003525. This paper describes objective technical results and analysis. Any subjective views or opinions that might be expressed in the paper do not necessarily represent the views of the U.S. Department of Energy or the United States Government. The United States Government retains, and the publisher, by accepting the article for publication, acknowledges that the United States Government retains a non-exclusive, paid-up, irrevocable, world-wide license to publish or reproduce the published form of this manuscript, or allow others to do so, for United States Government purposes.

Thank you to Wendy Calvin at University of Nevada Reno for use of the portable SWIR spectrometer utilized in this study. We would also like to thank Kelly Blake and Ormat Technologies INC for collaboration, sample access, and data share. We would also like to thank Paul Schwering.

DATA AVAILABILITY

The infrared reflectance spectroscopy data, and data interpretation spreadsheet are available as part of the data release titled "Basin and Range Investigation for Developing Geothermal Energy: Exploration Data" on the Geothermal Data Repository within the Gabbs Valley Exploration Data Package. The data can be accessed here: https://gdr.openei.org/submissions/1682

REFERENCES

Allis, R. G. (1990). Geophysical anomalies over epithermal systems. Journal of Geochemical Exploration, 36(1-3), 339-374.

Browne, P. R. L. (1978). Hydrothermal alteration in active geothermal fields. Annual Review of Earth and Planetary Sciences, 6(1), 229-248.

Calvin, W. M., & Pace, E. L. (2016). Alteration in geothermal drill core using a field-portable spectroradiometer. Geothermics, 61, 12-23.

Chambefort, I., Lewis, B., Simpson, M. P., Bignall, G., Rae, A. J., & Ganefanto, N. (2017). Ngatamariki geothermal system: Magmatic to epithermal transition in the Taupo volcanic zone, New Zealand. Economic Geology, 113(2), 319-346.

Clark, R. N., King, T. V., Klejwa, M., Swayze, G. A., & Vergo, N. (1990). High spectral resolution reflectance spectroscopy of minerals. Journal of Geophysical Research: Solid Earth, 95(B8), 12653-12680.

Craig, J. W., Faulds, J. E., Hinz, N. H., Earney, T. E., Schermerhorn, W. D., Siler, D. L., ... & Deoreo, S. B. (2021). Discovery and analysis of a blind geothermal system in southeastern Gabbs Valley, western Nevada, USA. Geothermics, 97, 102177.

Cumming, W. and Matson, G., 2021. Conceptual Challenges in Applying Geophysics to Geothermal Exploration in Indonesia. Invited Abstract In: Geophysics in Geothermal Energy – Today and Tomorrow. Society of Exploration Geophysics Workshop. 12-13 October 2021, Jakarta.

Delwiche, B. (2013). Exploration of the Wild Rose geothermal project, Mineral County, Nevada. In Nevada Petroleum and Geothermal Society Field Trip Guide: Geothermal and petroleum developments in several extensional basins of the central Walker Lane, Nevada (pp. 13-27).

Delwiche, B., Libbey, R., Folsom, M., Johnson, A., Murphy, J., & Zuza, R. (2023). Exploration history and conceptual model of the Dixie Meadows geothermal field, Nevada, USA. In Proceedings World Geothermal Congress 2023, Beijing, China, April 17-21.

DiPippo, R., Gutierrez-Negrin, L., Chiasson, A. (2025). Geothermal Power Generation Developments and Innovation, 2nd Edition. DiPippo, Gutierrez-Negrin, and Chiasson (ed.). Elsevier, ISBN: 978-0-443-24750-7654. 960 pp.

Downs, C., Schwering, P., Sewell, S., Winn, C., Hinz, N., Zimmerman, J., Blake, K., Sabin, A., Lopeman, J., Milton, A., Siler, D., & Cumming, W. (2023). Development of the Prospect Portfolio and initial surface exploration studies in the Basin & Range Investigations for Developing Geothermal Energy (BRIDGE) Project. GRC Transactions, 47.

Downs, C., Winn, C., Kraal, K., Folsom, M., Zimmerman, J., Sewell, S., Cumming, W., Milton, A., Hinz, N., Schwering, P., Sabin, A., & Lopeman, J. (2025). Basin & Range Investigations for Developing Geothermal Energy (BRIDGE). Final Technical Report. DOE Contract Number NA0003525.

Elders, W. A., Hoagland, J. R., McDowell, S. D., & Cobo, J. M. (1979). Hydrothermal mineral zones in the geothermal reservoir of Cerro Prieto. Geothermics, 8(3-4), 201-209.

ENVI software (6.1). Retrieved from https://www.l3harrisgeospatial.com/

Feucht, D., Gates, C., Selwood, R., Churchill, M., & Zuza, R. (2023). Magnetotelluric data acquisition in a high-noise environment: Results from the Steamboat Hills geothermal complex, Nevada, USA. GRC Transactions, 47.

Feucht, D., Delwiche, B., and Blake, K. (2024). High Resolution Geophysical Imaging of the Don A. Campbell Geothermal Resource: A Blind Sedimentary-Hosted Hydrothermal System in the Basin and Range, Nevada, USA. Poster presented at: American Geophysical Union Annual Meeting; December 10, 2024; Washington, D.C.

Folsom, M., Lopeman, J., Perkin, D., & Sophy, M. (2018, February). Imaging shallow outflow alteration to locate productive faults in Ormat's Brady's and Desert Peak fields using CSAMT. In Proceedings of the 43rd Workshop on Geothermal Reservoir Engineering (pp. 12-14). Stanford, CA, USA.

Folsom, M., Libbey, R., Feucht, D., Warren, I., & Garanzini, S. (2020, February). Geophysical observations and integrated conceptual models of the San Emidio geothermal field, Nevada. In Proceedings of the 45th Workshop on Geothermal Reservoir Engineering (pp. 21p). Stanford University, Stanford, CA, USA.

Folsom, M., Winn, C., Milton, A., Zimmerman, J., Blake, K., Sabin, A., Downs, C., Sewell, S., Kraal, K., Nale, S., & Huang, W. C. (2023). An early-stage exploration update on the Grover Point blind geothermal system in Dixie Valley, Nevada: Highlights of geophysics results and conceptual modeling. In Proceedings, 49th Workshop on Geothermal Reservoir Engineering (SGP-TR-227). Stanford University, Stanford, California.

Folsom, M., Sewell, S., Cumming, W., Zimmerman, J., Sabin, A., Downs, C., Hinz, N., Winn, C., Seiderman, B., & Schwering, P. (2024). A direct comparison of resistivity models from helicopter transient electromagnetic and magnetotelluric datasets collected over a blind geothermal system in East Hawthorne, Nevada, USA. GRC Transactions, 48.

Fournier, R. O. (1985a). The behavior of silica in hydrothermal solutions. In B. R. Berger, P. M. Bethke, & J. M. Robertson (Eds.), Geology and geochemistry of epithermal systems (Vol. 2). Society of Economic Geologists. https://doi.org/10.5382/Rev.02

Fournier, R. O. (1985b). Carbonate transport and deposition in the epithermal environment. In B. R. Berger, P. M. Bethke, & J. M. Robertson (Eds.), Geology and geochemistry of epithermal systems (Vol. 2). Society of Economic Geologists. https://doi.org/10.5382/Rev.02

Fournier, R. O. (1989). Geochemistry and dynamics of the Yellowstone National Park hydrothermal system. Annual Review of Earth and Planetary Sciences, 17(1), 13-53.

Glen, J. M., & Earney, T. E. (2024). GeoDAWN: Airborne magnetic and radiometric surveys of the northwestern Great Basin, Nevada and California. USGS Data Release. https://doi.org/10.5066/P93LGLVQ

Hassanzadeh, A. (2020). yxoos/ContinuumRemoval: Zenodo Release (1.0). Zenodo. https://doi.org/10.5281/zenodo.3612622

Henley, R. W., & Ellis, A. J. (1983). Geothermal systems ancient and modern: A geochemical review. Earth-Science Reviews, 19(1), 1-50.

Jowitt, S. M., Micander, R., Richards, M., Fisher, T., Reynolds, D., & Lu, C. (2024). The Nevada mineral industry 2023. Nevada Bureau of Mines and Geology Special Publication MI-2023, 96 p.

Kokaly, R. F., & Clark, R. N. (1999). Spectroscopic determination of leaf biochemistry using band-depth analysis of absorption features and stepwise multiple linear regression. Remote Sensing of Environment, 67(3), 267-287.

Kokaly, R. F., Clark, R. N., Swayze, G. A., Livo, K. E., Hoefen, T. M., Pearson, N. C., ... & Klein, A. J. (2017). USGS spectral library version 7 (No. 1035). US Geological Survey.

Kraal, K. O., Ayling, B. F., Blake, K., Hackett, L., Perdana, T. S. P., & Stacey, R. (2021). Linkages between hydrothermal alteration, natural fractures, and permeability: Integration of borehole data for reservoir characterization at the Fallon FORGE EGS site, Nevada, USA. Geothermics, 89, 101946.

Kraal, K. O. (2023a). Application of hydrothermal alteration mineral analysis to geothermal reservoir characterization for three geothermal fields in the western United States (Doctoral dissertation, University of Nevada, Reno).

Kraal, K. O., Ayling, B. F., DeOreo, S., & Calvin, W. (2023b). Infrared spectroscopy as a tool for hydrothermal alteration mineral analysis to support geothermal reservoir characterization at The Geysers, CA, USA. Journal of Volcanology and Geothermal Research, 445, 107968.

Kratt, C., Coolbaugh, M., Sladek, C., Zehner, R., Penfield, R., & Delwiche, B. (2008). A new gold pan for the West: Discovering blind geothermal systems with shallow temperature surveys. GRC Transactions, 32, 153-158.

Lederer, G., Jones, J., McPhee, D., Mauk, J., Seal, R., Campbell, K., Hammarstrom, J., Bedrosian, P., MacQueen, P., Graham, G., Solano, F., Case, G. and Pineault, D. (2024) USGS Annual Review 2023: Critical Minerals. Mining Engineering. 29-42

Lutz, S. J., Caskey, S. J., Mildenhall, D. D., Browne, P. R. L., & Johnson, S. D. (2002, January). Dating sinter deposits in northern Dixie Valley, Nevada—The paleoseismic record and implications for the Dixie Valley geothermal system. In Proceedings 27th Workshop on Geothermal Reservoir Engineering (pp. 284-290).

Lutz, S., Moore, J., Jones, C., Suemnicht, G., & Robertson-Tait, A. (2009, February). Geological and structural relationships in the Desert Peak geothermal system, Nevada: Implications for EGS development. In Proceedings 34th Workshop on Geothermal Reservoir Engineering.

Moore, J. N., Adams, M. C., & Anderson, A. J. (2000). The fluid inclusion and mineralogic record of the transition from liquid-to vapor-dominated conditions in the Geysers geothermal system, California. Economic Geology, 95(8), 1719-1737.

Orenstein, R., & Delwiche, B. (2014). The Don A. Campbell geothermal project. GRC Transactions, 38, 91-97.

Payne, J. F. (2013). Characterization of a blind geothermal prospect through LiDAR analysis and shallow temperature survey, Gabbs Valley, Nye and Mineral Co., NV (Master's thesis, University of Nevada Reno).

Pontual, S., Merry, N., & Gamson, P. (1997). Spectral interpretation field manual: Spectral analysis guide for mineral exploration 1.

Reyes, A. G. (1990). Petrology of Philippine geothermal systems and the application of alteration mineralogy to their assessment. Journal of Volcanology and Geothermal Research, 43, 279-309.

Rigby F. and Zebal, G., 1981. Case History on Geothermal-Well-Log Interpretation Surprise Valley, California. Los Alamos National Laboratory Report LA-8598-MS dated June 1981. Science Applications Final Report dated September 1980 for Contract 4-L29-77516-1.

Rimstidt, J. D., & Barnes, H. L. (1980). The kinetics of silica-water reactions. Geochimica et Cosmochimica Acta, 44(11), 1683-1699.

Savitri, K. P. (2024). Spectral analysis for geothermal exploration: A method investigation to bring the technology closer to geothermal community (PhD thesis, University of Twente, Faculty of Geo-Information Science and Earth Observation). https://doi.org/10.3990/1.9789036562034

Sewell, S., Cumming, W., Schwering, P., Hinz, P., Downs, C., Zimmerman, J., Bedrosian, P., Robinson, B., Murray, D., & Schultz, A. (2023). Using helicopter time-domain electromagnetic (HTEM) resistivity surveys with supporting geoscience data to target temperature gradient wells and discover hidden geothermal systems in the US Basin and Range. GRC Transactions, 47.

Sibson, R. H. (1987). Earthquake rupturing as a mineralizing agent in hydrothermal systems. Geology, 15(8), 701-704.

Sibson, R. H. (2000). Fluid involvement in normal faulting. Journal of Geodynamics, 29(3-5), 469-499.

Siler, D. L. (2023). Structural discontinuities and their control on hydrothermal systems in the Great Basin, USA. Geoenergy, 1(1), geoenergy2023-009.

Sillitoe, R. H. (2015). Epithermal paleosurfaces. Mineralium Deposita, 50(7), 767-793.

Simpson, M. P., & Rae, A. J. (2018). Short-wave infrared (SWIR) reflectance spectrometric characterization of clays from geothermal systems of the Taupo Volcanic Zone, New Zealand. Geothermics, 73, 74-90.

Stimac, J. (2023). Petrography as a cost-effective approach to understanding geothermal system evolution. GRC Transactions, 47, 1034911.

Thompson, A. J. B., Hauff, P. L., & Robitaille, A. J. (1999). Alteration mapping in exploration: Application of shortwave infrared (SWIR) spectroscopy. Society of Economic Geologists Newsletters, 39, 16–27.

Ussher, G., Harvey, C., Johnstone, R., & Anderson, E. (2000, May). Understanding the resistivities observed in geothermal systems. In Proceedings World Geothermal Congress (pp. 1915-1920). Kyushu, Japan.

Vest Christiansen, A., & Auken, E. (2012). A global measure for depth of investigation. Geophysics, 77(4), WB171-WB177.

Walters, M. A., Sternfeld, J. N., Haizlip, J. R., Drenick, A. F., & Combs, J. (1991). A vapor-dominated high-temperature reservoir at the Geysers, California. Geothermal Resources Council, Monograph on The Geysers Geothermal Field, Special Report No. 17.

Winn, C., Dobson, P., Ulrich, C., Kneafsey, T., Lowry, T., Akerley, J., ... & Bauer, S. (2021). Lost circulation in a hydrothermally cemented basin-fill reservoir: Don A. Campbell geothermal field, Nevada (No. SAND2021-7728C). Sandia National Lab. (SNL-NM), Albuquerque, NM (United States).

Winn, C., Dobson, P., Ulrich, C., Kneafsey, T., Lowry, T. S., Akerley, J., ... & Bauer, S. (2023). Context and mitigation of lost circulation during geothermal drilling in diverse geologic settings. Geothermics, 108, 102630.

Yang, K., Huntington, J. F., Browne, P. R., & Ma, C. (2000). An infrared spectral reflectance study of hydrothermal alteration minerals from the Te Mihi sector of the Wairakei geothermal system, New Zealand. Geothermics, 29(3), 377-392.

Yang, K., Browne, P. R. L., Huntington, J. F., & Walshe, J. L. (2001). Characterising the hydrothermal alteration of the Broadlands–Ohaaki geothermal system, New Zealand, using short-wave infrared spectroscopy. Journal of Volcanology and Geothermal Research, 106(1-2), 53-65.

Yang, K., Huntington, J. F., Gemmell, J. B., & Scott, K. M. (2011). Variations in composition and abundance of white mica in the hydrothermal alteration system at Hellyer, Tasmania, as revealed by infrared reflectance spectroscopy. Journal of Geochemical Exploration, 108(2), 143-156.